JOURNAL OF AIRCRAFT
Vol. 45, No. 6, November–December 2008

Numerical Investigations of Injection-Slot-Size Effect on the Performance of Coflow Jet Airfoils

Baoyuan Wang,* Bahaa Haddoukessouni,† Jonathan Levy,† and Ge-Cheng Zha‡
University of Miami, Coral Gables, Florida 33124

DOI: 10.2514/1.37441

Three coflow jet airfoils with twice-doubled injection-slot sizes are calculated using a Reynolds-averaged Navier–Stokes computational fluid dynamics solver with the one-equation Spalart–Allmaras model. At the same angle of attack, the twice-larger injection-slot-size airfoil passes the (about twice-greater) jet mass flow rate, with the momentum coefficients also nearly doubled. The coflow jet airfoil with the largest slot size has the least stall angle of attack. When the injection-slot size is reduced from the maximum by half, the stall angle of attack and the maximum lift coefficient are increased. When the injection-slot size is further reduced by half, the stall angle of attack is still increased, but the maximum lift coefficient is lower due to the smaller momentum coefficient. The trends of the stall angle of attack and maximum lift coefficient agree with the experiment. At low angles of attack, both the computed lift and drag coefficients agree fairly well with the experiment. At high angles of attack, the lift and drag are underpredicted. The reason may be that the Reynolds-averaged Navier–Stokes model cannot handle the turbulence mixing at high angles of attack.

Nomenclature

A	=	area
c	=	speed of sound
D	=	drag
d	=	distance to the closest wall
d_t	=	distance of the field point to the trip location
e	=	total energy per unit mass
F	=	reactionary force
J	=	Jacobian of transformation
L	=	lift
$\boldsymbol{l}$, $\mathbf{m}$, $\mathbf{n}$	=	normal vectors on ξ, η, and ζ surfaces with their magnitudes equal to the elemental surface areas and pointing to the directions of increasing ξ, η, and ζ
l_t, m_t, n_t	=	grid moving velocities
$\dot{m}$	=	mass flow rate
Pr	=	Prandtl number
Pr_t	=	turbulent Prandtl number
p	=	pressure
q_k	=	total heat flux in Cartesian coordinates
R	=	gas constant
Re	=	Reynolds number
R'	=	force from the airfoil surface integral
S	=	magnitude of vorticity in Cartesian coordinates
T	=	temperature
t	=	time
U, V, W	=	contravariant velocities in the ξ, η, and ζ directions
u, v, w	=	velocity components in the x, y, and z directions
$\mathbf{V}$	=	velocity vector
x, y, z	=	Cartesian coordinates
α	=	angle of attack
γ	=	ratio of specific heats
ΔU	=	difference of the velocities between the field point and the trip location
Δx_t	=	grid spacing along the wall at the trip location
θ	=	angle between slot surface and the line normal to the airfoil chord
μ	=	molecular viscosity
μ_t	=	turbulent viscosity
ν	=	kinematic viscosity
ξ, η, ζ	=	generalized coordinates
ρ	=	density
τ_{ik}	=	shear stress in Cartesian coordinates
ω_t	=	wall vorticity at the wall boundary-layer trip location

Subscripts

i, j, k	=	indices
L, R	=	left- and right-hand sides of the interface

Received 7 March 2008; revision received 11 June 2008; accepted for publication 24 June 2008.

*Ph.D. Candidate, Department of Mechanical and Aerospace Engineering. Member AIAA.

†Visiting Senior Undergraduate Student, Ecole d'Ingénieur en Modélisation Mathématique et Mécanique, France.

‡Associate Professor, Department of Mechanical and Aerospace Engineering; gzha@miami.edu. Senior Member AIAA.

I. Introduction

TO IMPROVE aircraft performance, innovative technology should be pursued to dramatically reduce the weight and fuel consumption of the aircraft and to significantly increase aircraft mission payload and stall margin. Both military and commercial aircraft will benefit from the same technology. Flow control is the most promising route to bring significant performance improvement to aircraft [1–7]. Recently, Zha et al. [8–11] developed a promising airfoil flow control technique using a coflow jet, which significantly increases lift, stall margin, and drag reduction.

The coflow jet airfoil is designed with an injection slot near the leading edge and a suction slot near the trailing edge on the airfoil suction surface. The slots are opened by translating a large portion of the suction surface downward. A high-energy jet is injected tangentially near the leading edge and the same amount of mass flow is drawn in near the trailing edge. The turbulent shear layer between the main flow and the jet causes strong turbulence diffusion and mixing under the severe adverse pressure gradient, which enhances lateral transport of energy from the jet to the main flow and allows the main flow to overcome the severe adverse pressure gradient and remain attached at high angles of attack (AOA). The high-energy jet induces high circulation and hence generates high lift. The energized main flow fills the wake and therefore reduces drag. The coflow jet (CFJ) airfoil achieves net-zero mass-flux flow control and can

significantly reduce the penalty to the propulsion system by dumping zero jet mass flow.

In [8,12], the CFJ airfoils with two different slot sizes are tested to compare the performance. It is observed that the larger slot size is more effective to reduce drag. The thin-slot-size airfoil is more energy-efficient to increase lift.

The first objective of this paper is to simulate the slot-size effect on the performance of the CFJ airfoils using computational fluid dynamics (CFD) and compare with the experiment. It is relatively easier to change the geometry in CFD simulation than in wind-tunnel tests to explore different geometries. Three CFJ airfoils with twice-doubled injection-slot sizes are studied by using a 3-D Reynolds-averaged Navier–Stokes (RANS) CFD solver. When the injection total pressures are about the same, the twice-larger injection area will allow about twice-greater injection mass flow rate as well as the momentum coefficients, which will affect the performance of the CFJ airfoils. The ultimate goal is to find the pattern of optimum geometry configuration for the CFJ airfoils.

The second objective of this paper is to examine CFD simulation capability for predicting the flowfield of the CFJ airfoils. A reliable CFD prediction is important to achieve optimum design of the CFJ airfoils and study the flow physics. Different from the previous work [10], which uses the unstructured CFD solver FLUENT to calculate the CFJ airfoil flows, an in-house structured CFD solver, Flow-Acoustics-Structure Interaction Package (FASIP), is used in the present computation. The FASIP code incorporates a low-diffusion Riemann solver, which is expected to have better accuracy for compressible flow than the pressure-based method used in FLUENT. Also, a structured-grid-block flow solver typically requires lower memory for a given mesh size and has better CPU efficiency because the line relaxation can be used. The RANS simulations of the CFJ airfoils in this paper show that it can predict the lift and drag fairly well at low AOA, but the deviation at high AOA is large. A more advanced turbulence modeling such as detached eddy simulation or large eddy simulation may be necessary to simulate the turbulence mixing at high AOA.

II. CFJ Airfoil Geometry

Figure 1 shows the baseline airfoil, NACA0025, and the other three airfoils with coflow jet slots. The chord length of the airfoil is 0.1527 m and the span is 0.3 m. The coflow jet airfoils are defined using the following convention: CFJ4dig-INJ-SUC, where 4dig is the same as the NACA 4-digit convention, INJ is the percentage of the injection-slot size to the chord length, and SUC is the percentage of the suction-slot size to the chord length. For example, the CFJ0025-065-196 airfoil has an injection-slot height of 0.65% of the chord and a suction-slot height of 1.96% of the chord. The suction-surface shape is a downward translation of the portion of the original suction surface between the injection and suction slots. The injection and suction slots are located at 7.11 and 83.18% of the chord from the leading edge. The slot faces are normal to the suction surface to make the jet tangential to the main flow.

The CFJ0025-131-196 airfoil is designed with an injection-slot size twice larger than that of the CFJ0025-065-196 airfoil to examine the effect of injection-slot size. The suction-slot size is unchanged. The slot locations are also the same as those of the CFJ0025-065-196 airfoil.

This paper simulates a new CFJ airfoil, CFJ0025-033-065, for which both the injection and suction sizes are half of the CFJ0025-065-196 airfoil. In other words, for the three CFJ airfoils shown in Fig. 1, the injection-slot sizes are doubled twice. The purpose is to study the injection geometry effect on the CFJ airfoil performance. The suction-slot-size design criterion is to be able to suck in the same injection mass flow without being choked.

The baseline airfoil, CFJ0025-065-196, and the CFJ0025-131-196 airfoil are tested in the wind-tunnel tests [12], and the experimental results are used for comparison with the CFD simulation in this paper.

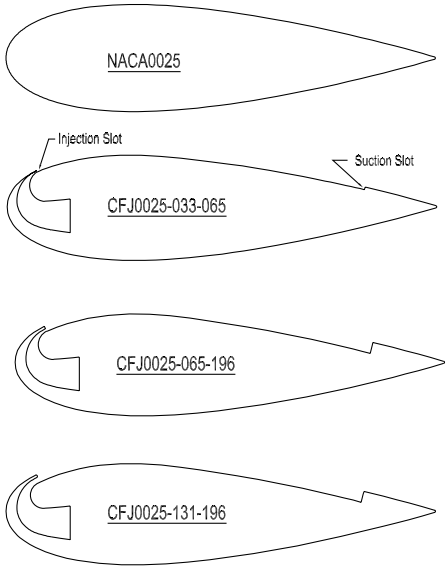

Fig. 1 Airfoil section of the baseline airfoil of the NACA0025 CFJ airfoil CFJ0025-065-196 and CFJ airfoil CFJ0025-131-196.

III. CFD Solver

A. Governing Equations

The governing equations are the RANS equations coupled with the S-A one-equation turbulence model [13]. In generalized coordinate system, the conservative form of the equations are given as follows:

$$\frac{\partial Q}{\partial t}+\frac{\partial \mathbf{E}}{\partial \xi}+\frac{\partial \mathbf{F}}{\partial \eta}+\frac{\partial \mathbf{G}}{\partial \zeta}=\frac{1}{Re}\left(\frac{\partial \mathbf{R}}{\partial \xi}+\frac{\partial \mathbf{S}}{\partial \eta}+\frac{\partial \mathbf{T}}{\partial \zeta}+\mathbf{D}\right) \tag{1}$$

where

$$Q=\frac{1}{J}\begin{bmatrix}\rho\\ \rho u\\ \rho v\\ \rho w\\ \rho e\\ \rho\tilde{\nu}\end{bmatrix} \tag{2}$$

$$\mathbf{E}=\begin{bmatrix}\rho U\\ \rho uU+l_x p\\ \rho vU+l_y p\\ \rho wU+l_z p\\ (\rho e+p)U-l_t p\\ \rho\tilde{\nu}U\end{bmatrix} \tag{3}$$

$$\mathbf{F}=\begin{bmatrix}\rho V\\ \rho uV+m_x p\\ \rho vV+m_y p\\ \rho wV+m_z p\\ (\rho e+p)V-m_t p\\ \rho\tilde{\nu}V\end{bmatrix} \tag{4}$$

$$\mathbf{G}=\begin{bmatrix}\rho W\\ \rho uW+n_x p\\ \rho vW+n_y p\\ \rho wW+n_z p\\ (\rho e+p)W-n_t p\\ \rho\tilde{\nu}W\end{bmatrix} \tag{5}$$

$$\mathbf{R} = \begin{bmatrix} 0 \\ l_k\tau_{xk} \\ l_k\tau_{yk} \\ l_k\tau_{zk} \\ l_k\beta_k \\ \frac{\rho}{\sigma}(\nu+\tilde{\nu})(\boldsymbol{l}\cdot\nabla\tilde{\nu}) \end{bmatrix} \tag{6}$$

$$\mathbf{S} = \begin{bmatrix} 0 \\ m_k\tau_{xk} \\ m_k\tau_{yk} \\ m_k\tau_{zk} \\ m_k\beta_k \\ \frac{\rho}{\sigma}(\nu+\tilde{\nu})(\mathbf{m}\cdot\nabla\tilde{\nu}) \end{bmatrix} \tag{7}$$

$$\mathbf{T} = \begin{bmatrix} 0 \\ n_k\tau_{xk} \\ n_k\tau_{yk} \\ n_k\tau_{zk} \\ n_k\beta_k \\ \frac{\rho}{\sigma}(\nu+\tilde{\nu})(\mathbf{n}\cdot\nabla\tilde{\nu}) \end{bmatrix} \tag{8}$$

$$D = \frac{1}{J}\begin{bmatrix} 0 \\ 0 \\ 0 \\ 0 \\ 0 \\ S_\nu \end{bmatrix} \tag{9}$$

where

$$\beta_k = u_i\tau_{ki} - q_k \tag{10}$$

$$S_\nu = \rho C_{b1}(1-f_{t2})\tilde{S}\,\tilde{\nu} + \frac{1}{Re}\left[-\rho\left(C_{w1}f_w - \frac{C_{b1}}{\kappa^2}f_{t2}\right)\left(\frac{\tilde{\nu}}{d}\right)^2 + \frac{\rho}{\sigma}C_{b2}(\nabla\tilde{\nu})^2 - \frac{1}{\sigma}(\nu+\tilde{\nu})\nabla\tilde{\nu}\bullet\nabla\rho\right] + Re[\rho f_{t1}(\Delta U)^2] \tag{11}$$

$$\begin{aligned} U &= l_t + \boldsymbol{l}\cdot\mathbf{V} = l_t + l_x u + l_y v + l_z w \\ V &= m_t + \mathbf{m}\cdot\mathbf{V} = m_t + m_x u + m_y v + m_z w \\ W &= n_t + \mathbf{n}\cdot\mathbf{V} = n_t + n_x u + n_y v + n_z w \end{aligned} \tag{12}$$

$$\boldsymbol{l} = \frac{\nabla\xi}{J}\,\mathrm{d}\eta\,\mathrm{d}\zeta, \qquad \mathbf{m} = \frac{\nabla\eta}{J}\,\mathrm{d}\xi\,\mathrm{d}\zeta, \qquad \mathbf{n} = \frac{\nabla\zeta}{J}\,\mathrm{d}\xi\,\mathrm{d}\eta \tag{13}$$

$$l_t = \frac{\xi_t}{J}\,\mathrm{d}\eta\,\mathrm{d}\zeta, \qquad m_t = \frac{\eta_t}{J}\,\mathrm{d}\xi\,\mathrm{d}\zeta, \qquad n_t = \frac{\zeta_t}{J}\,\mathrm{d}\xi\,\mathrm{d}\eta \tag{14}$$

When the grid is stationary, $l_t = m_t = z_t = 0$.

Because $\Delta\xi = \Delta\eta = \Delta\zeta = 1$ in the current discretization, Eqs. (13) and (14) are written as follows in the solver:

$$\boldsymbol{l} = \frac{\nabla\xi}{J}, \qquad \mathbf{m} = \frac{\nabla\eta}{J}, \qquad \mathbf{n} = \frac{\nabla\zeta}{J} \tag{15}$$

$$l_t = \frac{\xi_t}{J}, \qquad m_t = \frac{\eta_t}{J}, \qquad n_t = \frac{\zeta_t}{J} \tag{16}$$

The shear stress τ_{ik} and total heat flux q_k in Cartesian coordinates can be expressed as

$$\tau_{ik} = (\mu+\mu_t)\left[\left(\frac{\partial u_i}{\partial x_k} + \frac{\partial u_k}{\partial x_i}\right) - \frac{2}{3}\delta_{ik}\frac{\partial u_j}{\partial x_j}\right] \tag{17}$$

$$q_k = -\left(\frac{\mu}{Pr} + \frac{\mu_t}{Pr_t}\right)\frac{\partial T}{\partial x_k} \tag{18}$$

where μ is determined by Sutherland's law, and μ_t is determined by the S-A model:

$$\mu_t = \rho\tilde{\nu}f_{v1} \tag{19}$$

The kinematic viscosity ν is defined as

$$\nu = \frac{\mu}{\rho} \tag{20}$$

In Eqs. (6–8), (42), (17), and (18), the repeated subscripts i or k represent the coordinates x, y, and z following Einstein summation convention. Equations (17) and (18) are transformed to the generalized coordinate system in computation.

The sixth equation of the governing equations (1–9) is the S-A one-equation turbulence model [13]. The functions in the equation are given as

$$f_{v1} = \frac{\chi^3}{\chi^3 + C_{v1}^3} \tag{21}$$

$$\tilde{S} = S + \frac{\tilde{\nu}}{Re\kappa^2 d^2}f_{v2} \tag{22}$$

$$f_{v2} = 1 - \frac{\chi}{1+\chi f_{v1}} \tag{23}$$

$$f_w = g\left[\frac{1+C_{w3}^6}{g^6+C_{w3}^6}\right]^{\frac{1}{6}} \tag{24}$$

$$g = r + C_{w2}(r^6 - r) \tag{25}$$

$$f_{t1} = C_{t1}g_t\exp\left[-C_{t2}\frac{\omega_t^2}{\Delta U^2}\left(d^2 + g_t^2 d_t^2\right)\right] \tag{26}$$

$$g_t = \min\left(0.1, \frac{\Delta U}{\omega_t \Delta x_t}\right) \tag{27}$$

$$f_{t2} = C_{t3}\exp(-C_{t4}\chi^2) \tag{28}$$

where

$$\chi = \frac{\tilde{\nu}}{\nu} \tag{29}$$

$$S = \sqrt{\left(\frac{\partial w}{\partial y} - \frac{\partial v}{\partial z}\right)^2 + \left(\frac{\partial u}{\partial z} - \frac{\partial w}{\partial x}\right)^2 + \left(\frac{\partial v}{\partial x} - \frac{\partial u}{\partial y}\right)^2} \tag{30}$$

$$r = \frac{\tilde{\nu}}{Re\tilde{S}\kappa^2 d^2} \tag{31}$$

The constants in the S-A model are set to have the following values:

$$\sigma = \tfrac{2}{3}, \qquad C_{b1} = 0.1355, \qquad C_{b2} = 0.622, \qquad \kappa = 0.41$$
$$C_{v1} = 7.1, \qquad C_{w1} = C_{b1}/\kappa^2 + (1 + C_{b2})/\sigma$$
$$C_{w2} = 0.3, \qquad C_{w3} = 2, \qquad C_{t1} = 1$$
$$C_{t2} = 2, \qquad C_{t3} = 1.2, \qquad C_{t4} = 0.5$$

The full turbulent boundary-layer assumption is used in the computation by setting $C_{t1} = 0$ and $C_{t3} = 0$ to be consistent with the tripped boundary layer in the experiments. Because CFD solutions are obtained from the steady-state calculations based on the RANS model, the unsteady details of the shear-layer mixing entrainment and large coherent vortex structures are not able to be captured. The total pressure and total temperature are given at the injection-duct inlet as the boundary conditions.

To study the effect caused only by the geometry, the injection total pressure is iterated to match the experimental momentum coefficient. The static pressure at the suction-duct entrance is iterated to match the injection jet mass flow rate.

B. Scheme for Inviscid Flux

The low-diffusion E-CUSP (LDE) scheme given in [14] is used to evaluate the inviscid fluxes. The basic idea of the E-CUSP scheme is to split the inviscid flux into the convective flux E^c and the pressure flux E^p. With the one extra equation from the S-A model, the splitting is basically the same as the original scheme and is straightforward. In the generalized coordinate system, the flux $\mathbf{E}$ can be split as follows:

$$\mathbf{E} = E^c + E^p = \begin{pmatrix} \rho U \\ \rho u U \\ \rho v U \\ \rho w U \\ \rho e U \\ \rho \tilde{\nu} U \end{pmatrix} + \begin{pmatrix} 0 \\ l_x p \\ l_y p \\ l_z p \\ p\bar{U} \\ 0 \end{pmatrix} \tag{32}$$

where

$$\bar{U} = l_x u + l_y v + l_z w \tag{33}$$

The convective term E^c is evaluated as follows [14]:

$$E^c = \rho U \begin{pmatrix} 1 \\ u \\ v \\ w \\ e \\ \tilde{\nu} \end{pmatrix} = \rho U f^c, \qquad f^c = \begin{pmatrix} 1 \\ u \\ v \\ w \\ e \\ \tilde{\nu} \end{pmatrix} \tag{34}$$

Let

$$C = c\left(l_x^2 + l_y^2 + l_z^2\right)^{\frac{1}{2}} \tag{35}$$

Then the convective flux at interface $\frac{1}{2}$ is evaluated as

$$E^c_{\frac{1}{2}} = C_{\frac{1}{2}}\left[\rho_L C^+ f^c_L + \rho_R C^- f^c_R\right] \tag{36}$$

where the subscripts L and R represent the left- and right-hand sides of the interface.

The interface speed of sound is

$$C_{\frac{1}{2}} = \tfrac{1}{2}(C_L + C_R) \tag{37}$$

The following relations to express the formulations from $-\infty < M < \infty$ are used [14]:

$$C^+ = \alpha^+_L(1 + \beta_L)M_L - \beta_L M^+_L - M^+_{\frac{1}{2}} \tag{38}$$

$$C^- = \alpha^-_R(1 + \beta_R)M_R - \beta_R M^-_R + M^-_{\frac{1}{2}} \tag{39}$$

$$M_L = \frac{U_L}{C_{\frac{1}{2}}}, \qquad M_R = \frac{U_R}{C_{\frac{1}{2}}} \tag{40}$$

$$\alpha_{L,R} = \tfrac{1}{2}[1 \pm \mathrm{sign}(M_{L,R})] \tag{41}$$

$$\beta_{L,R} = -\max[0, 1 - \mathrm{int}(|M_{L,R}|)] \tag{42}$$

$$M^+_{\frac{1}{2}} = M_{\frac{1}{2}}\frac{C_R + C_L\Phi}{C_R + C_L} \tag{43}$$

$$M^-_{\frac{1}{2}} = M_{\frac{1}{2}}\frac{C_L + C_R\Phi^{-1}}{C_R + C_L} \tag{44}$$

$$\Phi = \frac{(\rho C^2)_R}{(\rho C^2)_L} \tag{45}$$

$$M_{\frac{1}{2}} = \beta_L\delta^+ M^-_L - \beta_R\delta^- M^+_R \tag{46}$$

$$M^\pm_{L,R} = \pm\tfrac{1}{4}(M_{L,R} \pm 1)^2 \tag{47}$$

$$\delta^\pm = \tfrac{1}{2}\{1 \pm \mathrm{sign}[\tfrac{1}{2}(M_L + M_R)]\} \tag{48}$$

The pressure flux E^p is evaluated as follows:

$$E^p_{\frac{1}{2}} = \begin{pmatrix} 0 \\ pl_x \\ pl_y \\ pl_z \\ p\bar{U} \\ 0 \end{pmatrix} = \begin{pmatrix} 0 \\ (\mathcal{D}^+_L p_L + \mathcal{D}^-_R p_R)l_x \\ (\mathcal{D}^+_L p_L + \mathcal{D}^-_R p_R)l_y \\ (\mathcal{D}^+_L p_L + \mathcal{D}^-_R p_R)l_z \\ \bar{C}_{\frac{1}{2}}(\mathcal{S}^+_L p_L + \mathcal{S}^-_R p_R) \\ 0 \end{pmatrix} \tag{49}$$

where

$$\mathcal{D}^\pm_{L,R} = [\alpha(1 + \beta) - \beta\mathcal{P}^\pm]_{L,R} \tag{50}$$

The pressure-splitting coefficient borrowed from Van Leer [15] is

$$\mathcal{P}^\pm_{L,R} = \tfrac{1}{4}(M_{L,R} \pm 1)^2(2 \mp M_{L,R}) \tag{51}$$

For the pressure term in the energy equation, the contravariant speed of sound $\bar{C}$ is consistent with $\bar{U}$ and is calculated as

$$\bar{C} = C - l_t \tag{52}$$

$$\mathcal{S}^\pm_{L,R} = [\bar{\alpha}^\pm(1 + \bar{\beta})M - \bar{\beta}\,\bar{M}]_{L,R} \tag{53}$$

where

$$\bar{M} = \frac{\bar{U}}{\bar{C}} \tag{54}$$

and $\bar{\alpha}$ and $\bar{\beta}$ are evaluated based on $\bar{M}$ using the formulations given in Eqs. (41) and (42). The use of $\bar{U}$, $\bar{C}$, and $\bar{M}$ in the pressure term for the energy equation is to take into account the grid speed so that the flux will transit from subsonic to supersonic smoothly. When the grid is stationary, $l_t = 0$, $\bar{C} = C$, and $\bar{U} = U$.

The LDE scheme can accurately resolve wall boundary-layer profiles and capture crisp shock profiles and exact contact surfaces [14] with low diffusion. The third-order MUSCL-type differencing of Van Leer is used with the LDE scheme. The viscous terms are discretized using second-order central differencing. The implicit

Gauss–Seidel line relaxation is used for time marching to achieve a high convergence rate.

C. Jet Effects on CFJ Airfoil Performance

By using a control volume analysis, Zha et al. [10] derived an expression for the force effect of the injection and suction jets on the CFJ airfoil. Based on Newton's third law, the momentum and pressure at the injection and suction slots produce a reactionary force, which must be taken into account in the drag and lift calculations. The expressions for these reactionary forces are given as

$$F_{x_{cfj}} = (\dot{m}_j V_{j1} + p_{j1} A_{j1}) \times \cos(\theta_1 - \alpha) - \gamma(\dot{m}_j V_{j2} + p_{j2} A_{j2}) \times \cos(\theta_2 + \alpha) \tag{55}$$

$$F_{y_{cfj}} = (\dot{m}_j V_{j1} + p_{j1} A_{j1}) \times \sin(\theta_1 - \alpha) - \gamma(\dot{m}_j V_{j2} + p_{j2} A_{j2}) \times \sin(\theta_2 + \alpha) \tag{56}$$

where the subscripts 1 and 2 stand for the injection and suction, respectively, and θ_1 and θ_2 are the angles between the injection and suction slots' surfaces and a line normal to the airfoil chord [10]. The total lift and drag on the airfoil can then be expressed as

$$D = R'_x - F_{x_{cfj}} \tag{57}$$

$$L = R'_y - F_{y_{cfj}} \tag{58}$$

where R'_x and R'_y are the surface integral of pressure and shear stress in the x (drag) and y (lift) directions. For the CFD simulation, the total lift and drag are calculated using Eqs. (57) and (58).

IV. Results and Discussion

The freestream Mach number is about 0.11 and the Reynolds number is about 3.8×10^5, which is in the laminar/transitional region. To make the boundary layer fully turbulent to mimic the realistic flight conditions, the airfoil leading edge is tripped to trigger the turbulence in the wind-tunnel tests. In CFD simulation, the boundary layer is assumed to be fully turbulent starting from the leading edge. The different boundary conditions between the experiment and CFD is that the CFD simulates the airfoil in an open field with no wind-tunnel wall. Such a difference is a common practice of CFD simulation and is expected to cause little effect on simulation accuracy. A typical 2-D computational mesh is shown in Fig. 2 with 5 blocks. The dimensions of the blocks in the tangential and radius directions are 33×49 (chamber), 97×97, 17×97, 23×97, and 59×193, respectively.

Figure 3 shows the momentum coefficients vs the AOA. In the wind-tunnel experiment, the injection total-pressure coefficients for the CFJ0025-065-196 and CFJ0025-131-196 are the same. Because the injection-slot size is increased by 2 times, the mass flow rate and the momentum coefficients are also about 2 times different, as shown in Fig. 3. The CFD computation matches the experimental momentum coefficients very well. For the CFJ0025-033-065 airfoil created in this paper, because no experiment is done, the momentum coefficients are determined by using the same injection total pressure as that of the CFJ0025-065-196 airfoil, which generates about half of the momentum coefficients of the CFJ0025-065-196 airfoil.

Figure 4 is the lift-coefficient comparison for the airfoils with the different slot sizes. The experiment shows that the CFJ0025-131-196 airfoil with the maximum slot size and momentum coefficients only generate slightly higher lift than the CFJ0025-065-196 airfoil before it stalls. The stall AOA and the maximum lift of the CFJ0025-131-196 airfoil is even less than that of the CFJ0025-065-196 airfoil, which has half the injection-slot size. The CFD simulations also predict the same trend. Quantitatively, the computed lift coefficients agree quite well with the experiment before AOA = 20 deg. When the AOA is greater than that, the CFD underpredicts the lift. It may be because that the RANS model cannot accurately predict the mixing process, which is inherently unsteady and may also have large vortex

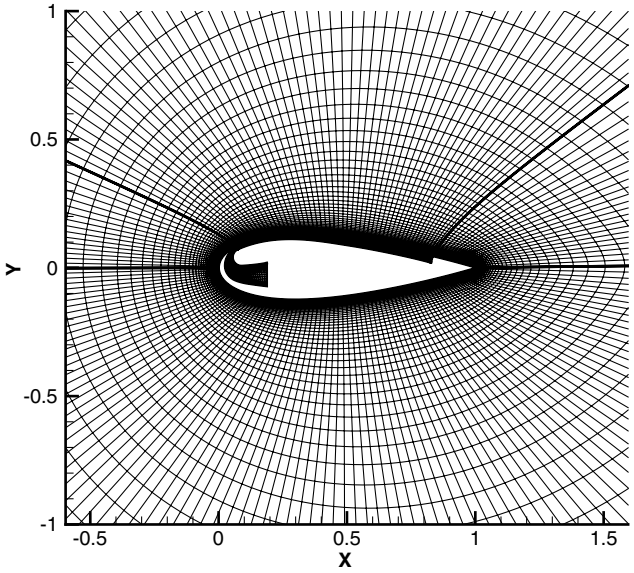

Fig. 2 Five-block grids for the CFJ airfoil.

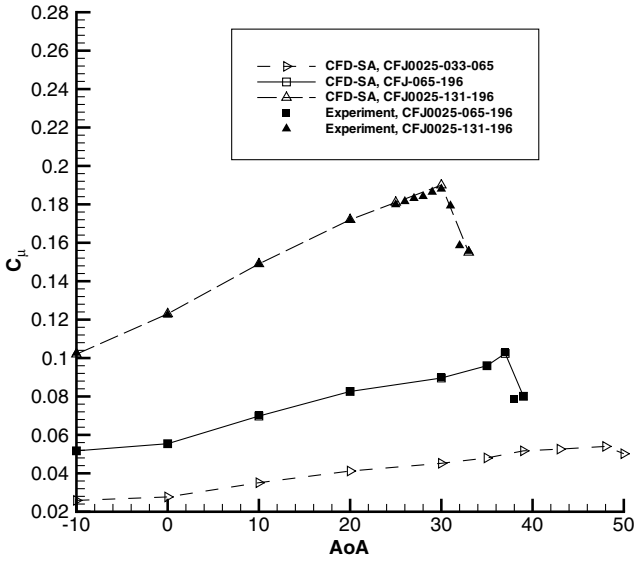

Fig. 3 Injection momentum coefficient of the CFJ airfoils with different injection-slot sizes.

structures generated. The stall AOA is predicted quite well, except that the trend of the stall is more gradual instead of being abrupt as shown in the experiment.

The CFD simulations of the CFJ0025-065-196 and CFJ0025-131-196 airfoil indicate that the smaller injection size airfoil has a higher maximum stall AOA and lift. This trend agree very well with the experiment. When the injection-slot size is further reduced by half as with the CFJ0025-033-065 airfoil, the stall AOA is also greater than that of the CFJ0025-065-196 airfoil, as shown in Fig. 4. However, the maximum lift of the CFJ0025-033-065 airfoil is lower than that of the CFJ0025-065-196 airfoil because the jet momentum or kinetic energy is lower.

Figure 5 is the drag coefficient of the CFJ airfoils with different injection-slot sizes. Similar to the lift prediction, the computed drags agree quite well with the experiment at low AOA. At high AOA, the drags are significantly underpredicted. Again, this may be attributed to the RANS turbulence model, which cannot well simulate the turbulence mixing at high AOA. In the experiment, the larger injection-slot airfoil has slightly lower minimum drag, but the computation does not generate such a difference.

A mesh refinement study for the CFJ0025-065-196 airfoil is done at AOA = 10 and 35 deg with the mesh size doubled in both directions. Both the lift and drag predicted with the refined mesh have

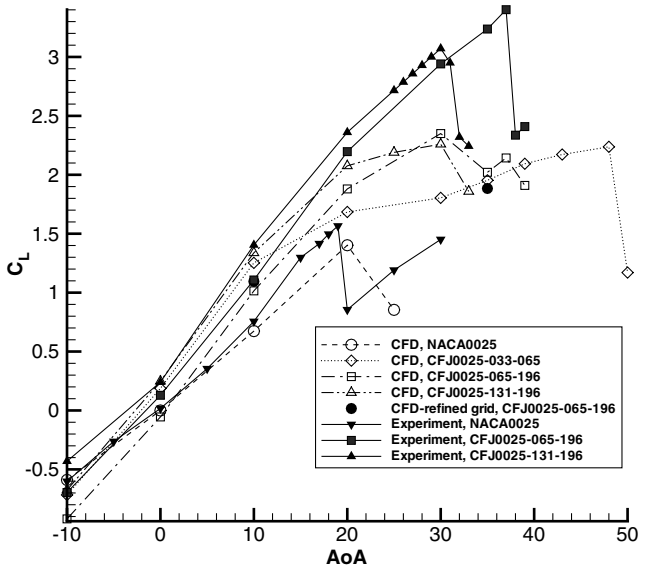

Fig. 4 Lift coefficient of the CFJ airfoils with different injection-slot sizes.

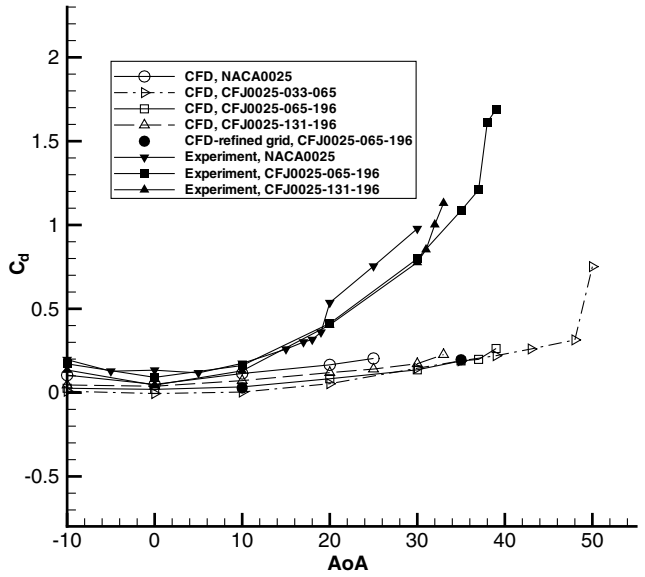

Fig. 5 Drag coefficient of the CFJ airfoils.

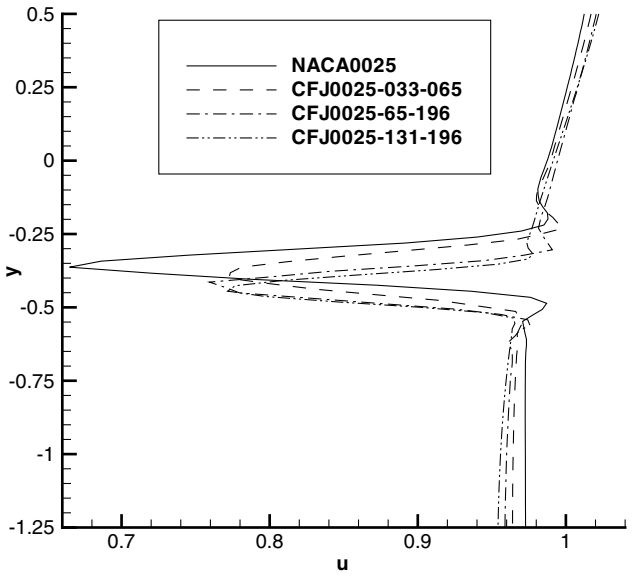

Fig. 6 Wake profile of the CFJ airfoil with injection.

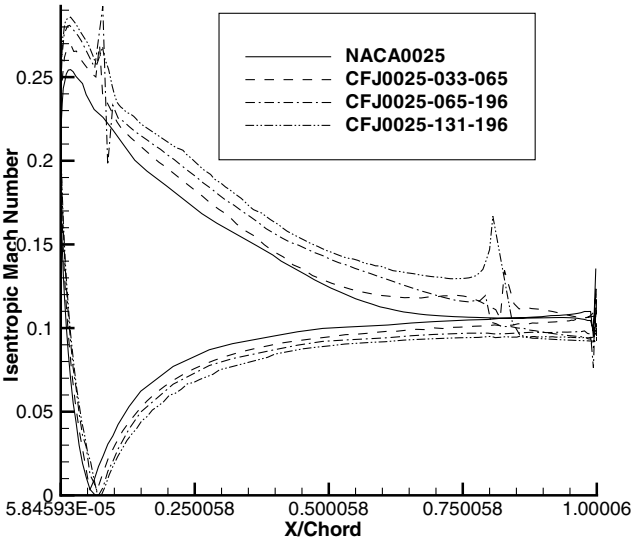

Fig. 7 Isotropic Mach number distribution on the surface of the CFJ airfoil with injection.

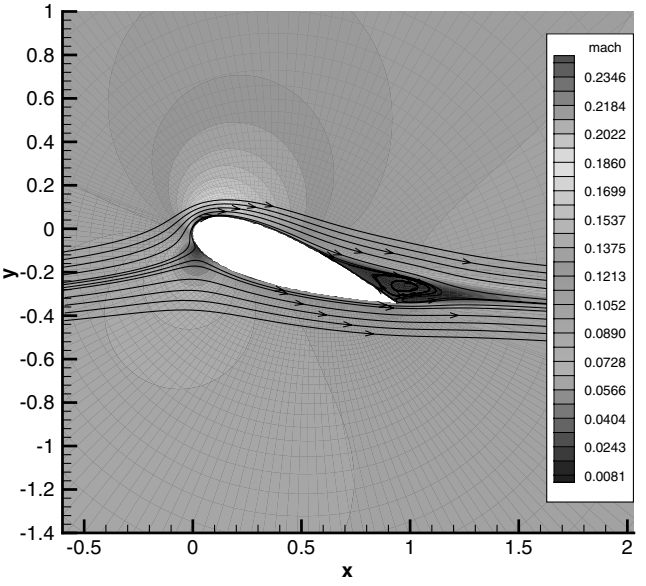

Fig. 8 Mach number contours of the NACA0025 airfoil at AOA = 20 deg.

little difference, as shown in Figs. 4 and 5, respectively. This means that the baseline mesh size used is sufficient for the solution convergence.

Figure 6 shows the wake profiles of the baseline NACA0025 airfoil and the three CFJ airfoils one chord length downstream of the airfoil trailing edge. It shows that the baseline NACA0025 airfoil has the deepest velocity deficit. The CFJ airfoils have shallower wake profiles due to the CFJ energizing the main flow. The shallower wake profile generates smaller drag than the baseline airfoil [11].

Figure 7 shows the surface isotropic Mach number for the airfoils at AOA = 20 deg. It can be seen that the surface loading, or the circulation, of the CFJ airfoils is much larger than that of the NACA0025 airfoil. The leading-edge suction peak Mach number of the CFJ airfoil is higher and the stagnation point is more downstream with the increase of the slot size. It can be seen that the injection locations are located downstream of the peak Mach number to make use of the adverse pressure gradient to enhance mixing [16].

Figures 8–11 shows the Mach number contours with streamlines of the baseline NACA0025 airfoil and the three CFJ airfoils at AOA = 20 deg, respectively. The baseline airfoil has a massive separation, which is consistent with the experiment [12]. The CFJ0025-033-065 airfoil also experiences a small separation at the

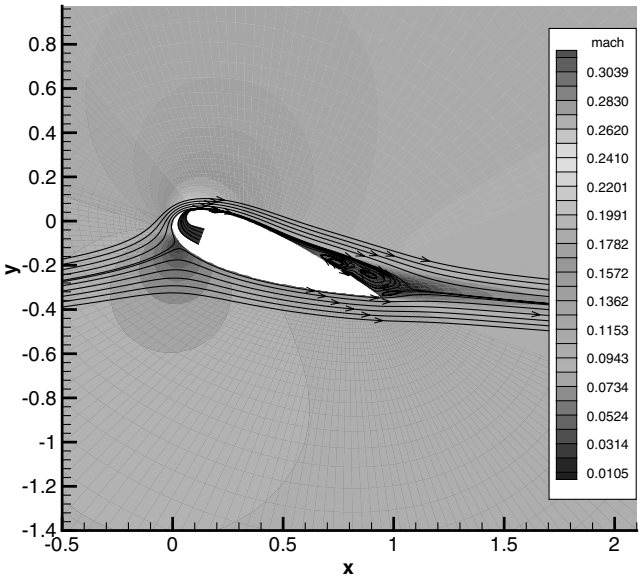

Fig. 9 Mach number contours of the CFJ0025-033-065 airfoil at AOA = 20 deg.

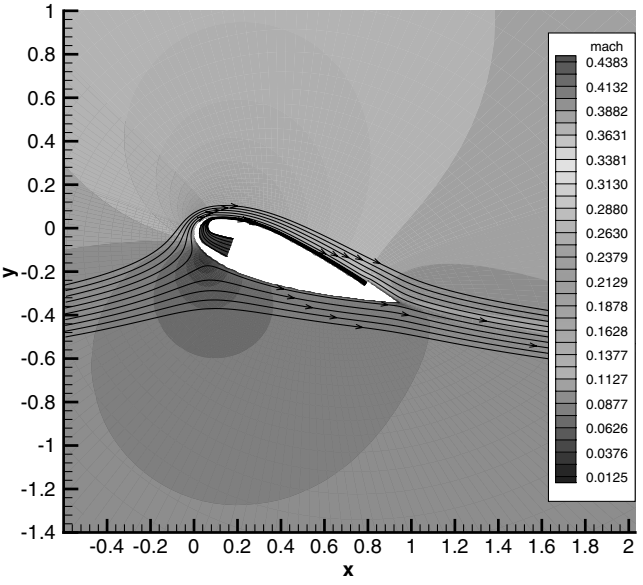

Fig. 10 Mach number contours of the CFJ0025-065-196 airfoil at AOA = 20 deg.

trailing edge because the jet momentum is not strong enough. Both the CFJ0025-065-196 and CFJ0025-131-196 airfoils do not have any separation at AOA = 20 deg due to the stronger CFJ, which is also the same as demonstrated in the wind-tunnel tests [8,12]. It is interesting to note that even though the CFJ0025-033-065 airfoil has the separation at AOA = 20 deg, the airfoil stall does not occur until AOA = 50 deg, as shown in Fig. 4. The airfoil may work under dynamically stable flow conditions, which may only be confirmed if unsteady simulation is conducted.

V. Conclusions

Three coflow jet airfoils with twice-doubled injection-slot sizes are calculated by using a RANS CFD solver with the one-equation Spalart–Allmaras (S-A) model. At the same angle of attack (AOA), the twice-larger injection-slot-size airfoil passes the (about twice-larger) jet mass flow rate, with the momentum coefficients also nearly doubled. However, just as with the trend shown in the wind-tunnel experiment, the CFJ0025-131-196 airfoil with the largest injection-slot size has the smallest predicted stall AOA. The

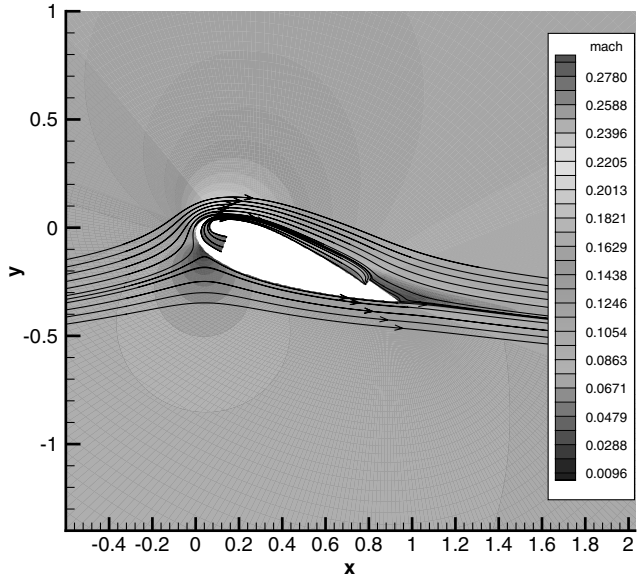

Fig. 11 Mach number contours of the CFJ0025-131-196 airfoil at AOA = 20 deg.

CFJ0025-065-196 airfoil with the injection-slot size reduced by half has higher stall AOA and maximum lift coefficient, which is consistent with the experiment. For the CFJ0025-033-065 airfoil, which is created in this paper with the injection-slot size further reduced by half of the CFJ0025-065-196 airfoil, the CFD simulation indicates that the stall AOA is further increased, but the maximum lift coefficient is lower due to the relatively weaker CFJ. The predicted lift and drag at low AOA agree fairly well with the experiment. At high AOA, both the lift and drag are underpredicted (particularly the drag). This may be attributed to the RANS turbulence model, which cannot capture the inherent unsteady mixing process of the CFJ airfoil at high AOA.

Acknowledgment

This research is supported under the U.S. Army Research Office and U.S. Air Force Office of Scientific Research grant 50827-RT-ISP monitored by Rhett Jefferier and Jerry Haire.

References

[1] Sellers, W. L. I., Singer, B. A., and Leavitt, L. D., "Aerodynamics for Revolutionary Air Vehicles," AIAA Paper 2004-3785, June 2003.

[2] Gad-el Hak, M., "Flow Control: The Future," *Journal of Aircraft*, Vol. 38, No. 3, 2001, pp. 402–418. doi:10.2514/2.2796

[3] Gad-el Hak, M., *Flow Control, Passive, Active, and Reactive Flow Management*, Cambridge Univ. Press, Cambridge, England, U.K., 2000.

[4] Anders, S., Sellers, W. L., and Washburn, A., "Active Flow Control Activities at NASA Langley," AIAA Paper 2004-2623, June 2004.

[5] Tilmann, C. P., Kimmel, R. L., Addington, G., and Myatt, J. H., "Flow Control Research and Application at the AFRL's Air Vehicles Directorate," AIAA Paper 2004-2622, June 2004.

[6] Miller, D., and Addington, G., "Aerodynamic Flowfield Control Technologies for Highly Integrated Airframe Propulsion Flowpaths," AIAA Paper 2004-2625, June 2004.

[7] Kibens, V., and Bower, W. W., "An Overview of Active Flow Control Applications at The Boeing Company," AIAA Paper 2004-2624, June 2004.

[8] Zha, G.-C., Paxton, C., Conley, A., Wells, A., and Carroll, B., "Effect of Injection Slot Size on High Performance Coflow Jet Airfoil," *Journal of Aircraft*, Vol. 43, No. 4, 2006, pp. 987–995. doi:10.2514/1.16999

[9] Zha, G.-C., and Paxton, C., "A Novel Flow Control Method for Airfoil Performance Enhancement Using Coflow Jet," *Applications of Circulation Control Technologies*, Progress in Aeronautics and AstronauticsVol. 214, AIAA, Reston, VA, 2006, pp. 293–314.

[10] Zha, G.-C., Gao, W., and Paxton, C., "Jet Effects on Coflow Jet Airfoil

Performance," *AIAA Journal*, Vol. 45, No. 6, 2007, pp. 1222–1231. doi:10.2514/1.23995

[11] Zha, G.-C., Carroll, B., Paxton, C., Conley, A., and Wells, A., "High Performance Airfoil Using Coflow Jet Flow Control," *AIAA Journal*, Vol. 45, No. 8, 2007, pp. 2087–2090. doi:10.2514/1.20926

[12] Zha, G.-C., Carroll, B., Paxton, C., Conley, A., and Wells, A., "High Performance Airfoil with Coflow Jet Flow Control.," AIAA Paper 2005-1260, 2005.

[13] Spalart, P., and Allmaras, S., "A One-equation Turbulence Model for Aerodynamic Flows," AIAA Paper 92-0439, 1992.

[14] Zha, G.-C., Shen, Y., and Wang, B., "Calculation of Transonic Flows Using WENO Method with a Low Diffusion E-CUSP Upwind Scheme," 46th AIAA Aerospace Sciences Meeting, AIAA Paper 2008-0745, Reno, NV, Jan. 2008.

[15] Van Leer, B., "Flux-Vector Splitting for the Euler Equations," *Lecture Notes in Physics*, Vol. 170, 1982, pp. 507–512. doi:10.1007/3-540-11948-5_66

[16] Greitzer, E., Tan, C., and Graf, M., *Internal Flows*, Cambridge Univ. Press, Cambridge, England, 2004.